Mapping fractures with GPR: A case study from Turtle Mountain

Ulrich Theune[1], Dean Rokosh[2], Mauricio D. Sacchi[1], and Douglas R. Schmitt[1]

ABSTRACT

Ground-penetrating radar (GPR) surveys were acquired of rocks on the highly fractured summit of Turtle Mountain in Canada. In 1903 a disastrous rock slide occurred at Turtle Mountain and it still poses a geologic hazard. Dips, shapes, and penetration depths of fractures are important parameters in slope-stability analysis. Determination of fracture orientation at Turtle Mountain has been based mostly on areal geologic mapping and, most recently, on data collected from boreholes. The purpose of GPR surveys was to test, confirm, and extend information about fractures and bedding planes. Data acquisition was complicated by the rough terrain; because slopes are steep and uneven. This also complicated analysis of the data. Measurement of in situ velocity — an important value for migration — was impossible. Instead, data were migrated with different velocities and data results were chosen that were considered to be reasonable. Analysis and interpretation of the data, resulted in confirmation and extension of the a priori information on orientations of fractures and bedding planes at Turtle Mountain. Despite the rough terrain and highly fractured rock mass, GPR surveys provide reliable information about the shapes and density of fractures — information important for slope-stability evaluation. The most reliable migration results obtained for velocities were considerably less than the standard velocities recorded for limestone, the dominant lithofacies at Turtle Mountain. We interpret this observation as an indicator of water within the rock. However, thorough investigation of this conclusion remains a project for future work.

INTRODUCTION

Application of ground-penetrating radar (GPR) is similar to application of the seismic method, in that both employ the imaging of reflectors within the earth. GPR has gained popularity in near-surface imaging because of its high vertical and lateral resolution capabilities and is used often in hydrogeologic and environmental studies (Davis and Annan, 1989; Zeng and McMechan, 1997; Moldoveanu-Constantinescu and Stewart, 2004), in forensic studies (Hammon et al., 2000), and in archaeological studies (Goodman et al., 1995). This method has frequently been applied in geotechnical studies — for example, to map fractures and faults in the subsurface. Mapping of fractures in plutonic rocks as an application of GPR was described by Stevens et al. (1995). Grasmueck (1996) reported an application of 3D GPR surveys to imaging of the fracture system in a gneiss quarry. Grodner (2001) summarized delineation of fractures in deep mines, and Rashed et al. (2003) reported results of GPR characterization of near-surface faults in Japan. Willenberg et al. (2004) described borehole radar measurements to determine the penetration depths of fractures in the Swiss Alps.

In this paper, we describe application of GPR surveys to image the internal structure of highly fractured rocks at the summit of Turtle Mountain, Alberta, Canada. Turtle Mountain was the location of the Frank Slide in 1903 (Figure 1). Because Turtle Mountain is geomechanically unstable, rock falls are still a hazard. To assess the risk of rock slides, knowledge of the complex fracture system is important (Hoek and Bray, 1981). Of particular interest is the determination of subsurface shapes of fractures, because dips and depths of fractures are important variables in the construction of geomechanical models for stability analysis.

Turtle Mountain has attracted considerable attention recently. It is the focus of a monitoring-research project that combines information about geology, geophysics, and geomechanics. Monitoring of deep fractures in the mountain had been based on strain gauges installed in deep cracks and on periodic aerial photography. In the current phase, the monitoring program to detect small movements within the mountain is extended by observation systems for microseismology, by continuous GPS measurements, and by laser interferometry. Additionally, extensive areal geologic mapping of fractures at the surface was conducted on the mountain's summit during 2004. To augment this information by investigating deep fractures, a bore-

hole approximately 60-m deep was drilled in 2004 (Spratt and Lamb, 2005). However, evidence from the areal geologic maps and from analysis of aerial photographs tends to draw emphasis to the steeply dipping geologic features, whereas borehole geophysics allows for point-wise detection of potentially dangerous deep fractures, which of course are not made obvious by areal geologic mapping. Information from surface mapping and from the borehole provides data for only a small part of Turtle Mountain, but surface geophysical measurements provide complementary information over a larger area. We carried out several ground-penetrating-radar surveys on Turtle Mountain to map the near-surface structure of the summit at locations where large fractures cut deep into the mountain. These localities were judged to be where slides are likely to occur.

HISTORICAL AND GEOLOGIC BACKGROUND

When the summit of Turtle Mountain collapsed in the early morning of April 29, 1903, approximately 30 million m³ of the east limb of the Turtle Mountain anticline slid, and destroyed the southern part of the town Frank. Known as the Frank Slide, this event lasted for about 100 s and covered approximately 3 km² with rubble diverging 14-m thick. The summit of Turtle Mountain still is approximately 900 m above the valley. Figure 2a and b shows the present state of Turtle Mountain. Figure 2a shows the rock-slide area, South Peak
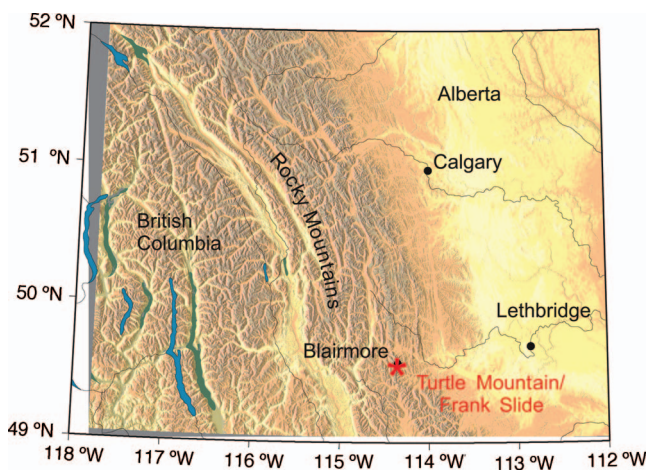

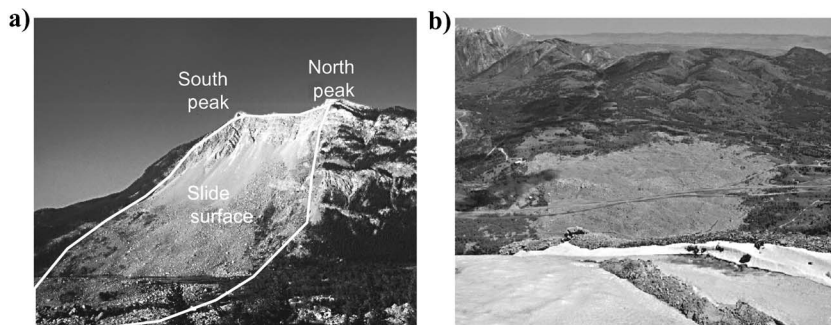Figure 1. Map of parts of southern Alberta and British Columbia, Canada (boundary not shown).

Figure 2. Views of Turtle Mountain after the rock avalanche. (a) The slide as seen from the east. (b) A view of the slide deposit area as seen from the top of the mountain looking eastward. The study area is at the summit, on the back side of Figure 2a.

and North Peak, and Figure 2b shows the slide as seen from South Peak eastward.

Figure 3 is a general geologic map of bedrock of the Turtle Mountain area. Our purpose is to describe briefly the geology of the area, and to concentrate on geology relevant to GPR data collection and interpretation — especially trends of joints and fractures. The oldest Paleozoic strata, in the central part of the anticline, are beds of the Banff Formation (Mississippian) (Figure 3), which are shaley limestones that underlie coarse-grained limestone of the Livingstone Formation. The abundantly fractured Livingstone Formation outcrops in the area of the survey (Figure 3) and is the only formation imaged by GPR surveys. Overlying the Livingstone is the Mount Head Formation (Figure 3), which is comprised of interbedded shaley limestone and dolomite. Limestone and dolomite (Pennsylvanian/Permian) of the lower part of the Rocky Mountain Formation overlie the Mount Head Formation (Figure 3). Sandstone and siltstone of the upper Rocky Mountain Formation are the youngest set of Paleozoic strata in the sequence (Benko and Stead, 1998).

The Turtle Mountain thrust fault separates Paleozoic strata from the underlying Jurassic sandstones and shales of the Fernie Formation (Figure 3a). Triassic strata are absent, although Benko and Stead (1998) suggested that strata of the Triassic Spray River Formation sediments may be included in the Rocky Mountain Formation, as mapped in the area of study. Overlying the Fernie Formation is the Kootenay Group (upper Jurassic/lower Cretaceous) (Figure 3), which consists mainly of massive sandstone with interbedded shale and coal. The youngest Mesozoic rocks in this area are lower cretaceous siliciclastics of the Blairmore Group (Figure 3).

The Turtle Mountain anticline is a fault-bend fold. During the Laramide orogeny, Mississippian carbonate rocks of the Rundle Group were thrust over weaker, and at present nearly vertical siliciclastic strata and coal of the Jurassic Fernie Formation (Benko and Stead, 1998). A minor thrust fault is above the main thrust (Figure 3); it has disturbed strata of the upper Rundle Group along the east limb of the anticline. Folding of the rock mass also created fracture zones that transmitted water through the carbonate rocks; networks of caves and smaller solutions cavities were eroded within the mountain. Glaciation exposed the mountain's weak foundation of mesozoic rocks. When the ice melted, the lower part of the steep valley wall slope became gravitationally unstable. Additionally, seams of coal were exposed in the lower slopes of Turtle Mountain (Figure 3). Underground mining of the coal was established quickly and accelerated by completion of a railway. Mining tunnels may additionally have diminished the marginal stability of Turtle Mountain. Undoubtedly the mountain was near its stability limit prior to the slide. Nonetheless, the Turtle Mountain rock slide was caused mostly by the generally unstable geologic structure of the mountain with its network of deep fractures (Benko and Stead, 1998).

During the winter of 1902–1903, a thick, heavy snow pack accumulated on Turtle Mountain's summit. April 1903 was unseasonably warm, and much of the snow melt went into the fracture network. During the night of April 28 the temperature dropped suddenly. This sequence of events is assumed: Water froze in fractured bedrock, the cracks expanded, and eventually the expansion triggered the collapse of Turtle Mountain (Benko and Stead, 1998). According to Cruden and

Krahn (1973, p. 582), "…the slide mass lay on the steeply eastward dipping limb of the anticline and the crest of the fold lay very close to the crown of the slide. The slide probably took place on bedding surfaces with the orientation of the scarp and lateral margins of the slide controlled by joint sets."

To prevent casualties resulting from rock slides, the Alberta Geological Survey initiated a detailed geotechnical hazard assessment of Turtle Mountain's south peak in September 1999 (Read et al., 2000; Stewart et al., 2004). The network of deep subvertical fissures still presents a potential danger of rock slides. With regard to stability of the south peak, Allan (1931, 1933) estimated that approximately 5 million m^3 form a danger zone. Considering the history of the 1903 rock slide, knowledge of the shapes and trends of fractures at depths on the mountain slope is important to estimate the amount of rock mass likely to collapse. A particularly important question is whether fractures penetrate the mountain and resurface (For example, see Figure 3b, fracture F1) or whether the deep fractures are approximately parallel to dip of the slope (Figure 3b, fracture F2). The purpose of our surveys was to provide an approximate image of the near-surface structural geology — especially the trends of fractures and joints — for development of geomechanical models of Turtle Mountain.

Locations of the four GPR lines A′A, B′B, C′C, and P′P are shown in Figure 4. Data for line PP′ were acquired along the crest of Turtle Mountain, where two major fractures were crossed at the summit. These fractures are labeled Crack 1 and Crack 2. Lines A′A and B′B were the main part of our survey. These profiles were acquired at the west slope; both cross Crack 1 and Crack 2. Line C′C was conducted on a steep slope near the mountain's crest. Additionally, differential GPS measurements were taken to determine the slope of the mountain along lines A′A and B′B. Locations of faults that penetrated to the surface along lines A′A and B′B were mapped, to identify fractures discernible in the processed field data.

Figure 4 also shows stereonet projections of poles to fracture patterns. A description of stereonets and their application to interpretation of fracture is described by Marshak and Mitra (1988), among others. Values within the stereonets represent the number of measured strike-and-dip sets. The sets are converted to poles to fracture planes and plotted on the stereonet. The summit of south peak is located in the upper left quadrant of the photograph (Figure 4). Along line B′B in the aerial photograph, the terrain slopes approximately 30° southwestward, along the west limb of the anticline, whereas bedding planes in the heavily fractured rock at the surface dip 55° to 60°, approximately southwestward. At issue and relevant to GPR data, is the dip of the main fractures in the subsurface, relative to dip of the bedding and slope of the surface. At the surface, the large open fractures designated as Crack 1 and Crack 2 have apparent vertical dips, as indicated on the stereonet (Big open cracks) and are as wide as 1 to 2 m (Figure 5). Trends of these cracks in the bottom-left quadrant of the photograph are northwestward, traversing slightly oblique to the mountain crest and subparallel to the dip direction (Figure 4). In the left-central part of Figure 4 the cracks trend more northerly, essentially parallel to the mountain crest. Whether these major fractures are vertical in the subsurface, or inclined, is not known. Spratt and Lamb (2005) described recent work on the interpretation of borehole data collected in the area shown in the top left quadrant of the photo. The fractures are interpreted as being large and open at depth; walls of the fractures are believed to be open, by 1 to 2 cm. They seem to strike northeasterly and dip more than 60°. Spratt and Lamb (2005) suggested that these major subsurface fractures may be

connected to large fractures in rocks at the surface, visible in Figure 4 (Cracks 1 and 2). Stereonets N = 32 and N = 42 in Figure 4 show poles that indicate fractures that are not vertical at the surface. These data suggest surface fractures that trend northeastward and dip about 45° S. Fractures also have been described along bedding planes (Cruden and Krahn, 1973). In the middle right quadrant of Figure 5a.
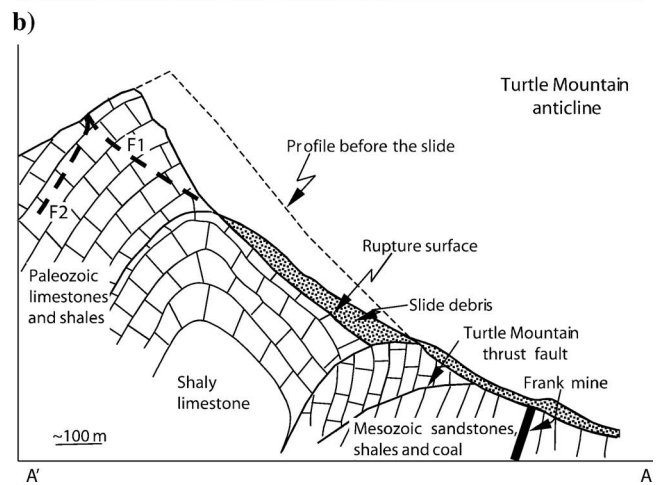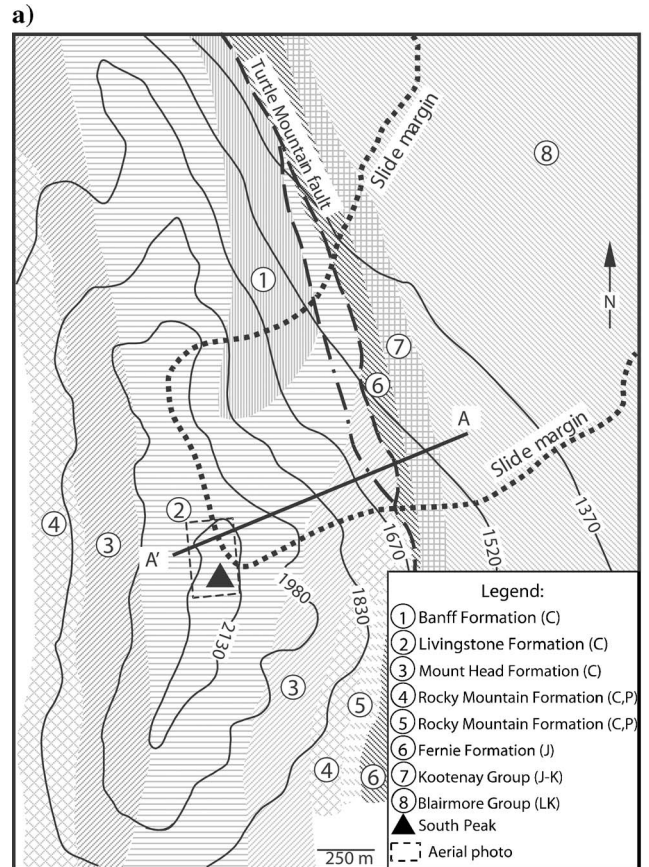

Figure 3. (a) Geologic map of the Turtle Mountain area. Contour lines show elevation in meters. The approximate section covered by Figure 4 is indicated by the dashed rectangle around South Peak. (b) Schematic cross section follows the profile AA′. F1 and F2 indicate two orientations of deep fractures within the mountain. (After Cruden and Krahn, 1973.)
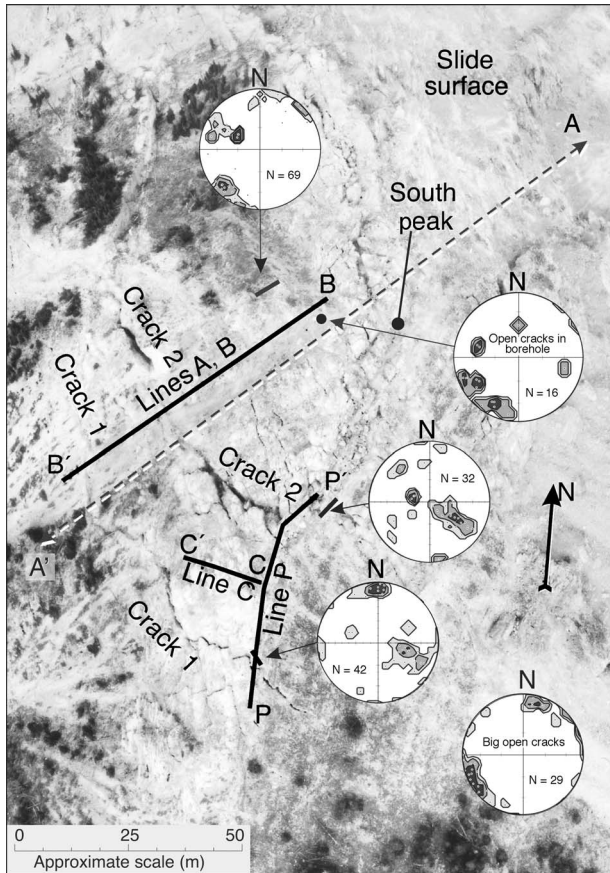
Figure 4. Aerial photograph of summit, Turtle Mountain. The line labeled B′B shows the location of one of three profiles; lines C′C and PP′ show locations of the remaining two profiles. Lengths of profiles are approximate. Orientations of sets of fractures are shown by stereonet diagrams. Three diagrams show orientations of fractures at sites indicated by thick black lines. One diagram shows orientations of open cracks in the borehole, and one shows orientations of large open cracks at the summit of Turtle Mountain. Dashed line AA′ indicates the approximate position of schematic cross section AA′ in Figure 3b. Horizontal scale is approximate. (Photograph and stereonet diagrams courtesy of the Government of Alberta.)

Crack 1 seems to follow joint sets, but at some localities elsewhere it cuts across joints. Cruden and Krahn (1973) observed two orthogonal joint sets, each perpendicular to bedding planes (joints of one set are closely spaced and strike parallel to strike of the bedding; the other set strikes parallel to dip). Cruden and Krahn (1973) and Benko and Stead (1998) also observed gaping tension cracks parallel to strike near the crown of the summit at Turtle Mountain. The cracks showed some indication of vertical displacement of bedrock. Striations are evident on bedding surfaces (Cruden and Krahn, 1973).

Trends of the joints and fractures are relevant to their detection on GPR lines A′A, B′B, C′C and PP′; some of these discontinuities cannot be imaged on the surveys. Surveys A′A and B′B are congruent and trend northeastward (Figure 4) oblique to the crest of the mountain. Major cracks 1 and 2 cross survey lines A′A and B′B approximately perpendicular to the lines trend. This is the best angle for imaging discontinuities, unless the plane of the discontinuity is vertical. Orthogonal joints, respectively parallel to strike and dip of the bedding, cross surveys A′A and B′B at roughly 45 degrees, as do tension fractures that parallel the crest of the anticline. The orientation of survey line C′C (Figure 4) is approximately the direction of dip of bedding; the line was located between Crack 1 and Crack 2. Tension fractures and the closely spaced sets of joints that parallel bedrock strike may be detectable on survey line C′C, and sets of joints parallel to the survey and to bedding dip may be imageable if the fracture planes cross the survey at relatively shallow angles to the surface. Lastly, survey PP′ roughly parallels the strike of the bedding, although an elbow in the line is at about midpoint. Cracks 1 and 2 cross line PP′ roughly perpendicular to the survey, as do dip-parallel joints. Joint sets that parallel the survey line (strike-parallel joints) may not be imageable at the north end of the line, but they cross the south end of the survey obliquely.

ACQUISITION AND PROCESSING OF DATA

During the compilation of GPR measurements, a pair of radar antennae is moved along a line in small increments: Data are recorded serially in this manner. Traces are combined into an image called a radargram, which can be considered as the equivalent of a nonmigrated stack of zero-offset traces in seismic data. From a source antenna at the surface, a high-frequency electromagnetic wave is emitted into the ground. Where waves encounter subsurface discontinuities (such as differences in dielectric properties between beds of sediment or rock, or buried objects), a portion of the signal is reflected to the surface. There it is recorded by a second antenna near the source. Therefore, GPR measurements can be considered as being the electromagnetic equivalent of zero-offset seismic experiments.

Propagation velocities of electromagnetic waves depend on the electrical properties of the subsurface material. For materials with negligible electrical conductivity, σ, and high frequencies (in the range of 10–1000 MHz) dispersion effects are small, and velocity depends mainly on the dielectric constant, ϵ (Davis and Annan, 1989):
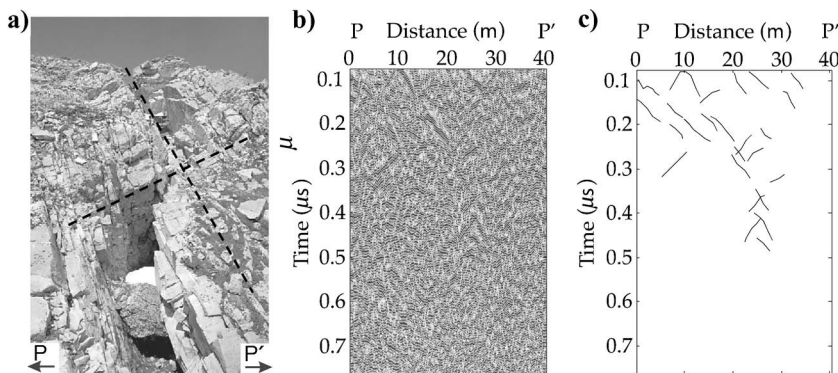
Figure 5. (a) Photograph of Crack 1, looking westward (see location of Crack 1 in Figure 4). Beds of limestone strike toward the upper left-hand part of the photograph, and dip steeply toward the right-hand side of the photograph. The two fracture systems are indicated by red lines. (b) Signatures of Crack 1 and Crack 2 are detectable at distances of approximately 10 and 23 m. (c) Delineation of some of the strong reflectors in the GPR data.

$$V(\omega) = \frac{1}{\sqrt{\mu_o \epsilon}\left(1 + \frac{1}{8}\frac{\sigma^2}{\omega\epsilon}\right)} \tag{1a}$$

and

$$V \approx \frac{c}{\sqrt{\epsilon_r}} \text{ for } \sigma \approx 0, \tag{1b}$$

where c is the speed of light in vacuum, μ_0 is the magnetic permeability constant, and $\epsilon = \epsilon_o \epsilon_r$, with ϵ_o being the free-space permittivity, and ϵ_r being the material-specific relative dielectric constant.

The maximal depth of penetration of homogeneous rock can be estimated by evaluating the skin depth d_s, which is related to conductivity and source frequency f, according to Knödel et al. (1997):

$$d_s = \sqrt{\frac{2}{\mu_0 \sigma f}}. \tag{2}$$

Skin depth is the depth at which the signal amplitude A has decreased to a fraction of e^{-1} of its initial value ($A = A_o/e$, where A_o is the initial amplitude).

Table 1 was compiled after Landau-Boernstein (1982); Davis and Annan (1989); and Guéguen and Palciauskas (1994); it shows the relevant properties of some common near-surface earth materials. We also include calculated velocities (Equation 1a) and skin depth (Equation 2) as a function of frequency. As mentioned previously, the rocks investigated in this experiment are mainly limestone. For the sake of comparison, we include values representative of other types of rock that may be present at Turtle Mountain (Table 1). We also include values for quartz, and for calcite, the latter of which is the principal component of limestone. Although the dielectric constants of these minerals are similar to those of sandstone and limestone, their electrical conductivities are negligible, relative to these of the rock material. Therefore, we did not calculate the skin depths for these pure minerals, because the values would be very large and not representative, and thereby not suited for realistic applications. Skin depth depends strongly on the frequency used. It is larger for low-frequency antennae; therefore, such antennae are preferable for deeper exploration of the subsurface.

Values in Table 1 are representative only of homogeneous media. For porous or fractured media, effective-media theories can be used to determine a representative value for the electromagnetic velocity. Such macroscopic velocities will be needed for validation of velocities used in migration trials that were applied to the data, prior to interpretation. Calculation of effective-medium values for electrical conductivity and dielectric permittivity requires knowledge of various parameters, such as properties of components of the effective medium and microstructure of the pore space (Guéguen and Palciauskas, 1994). As many of these parameters were unknown to us, we assumed simplified models for calculation of macroscopic properties of an effective medium, consisting of limestone, water, and air.

The effective velocity was calculated in two steps. First, effective values were calculated for dielectric permittivity ϵ^* and electrical conductivity σ^*. The effective velocity follows according to Equation 1a. For a three-component medium such as limestone, water, and air, the effective dielectric permittivity can be determined by a self-consistent approximation

$$\sum_i \varphi_i \frac{\epsilon_i - \epsilon^*}{\epsilon_i + 2\epsilon^*} = 0, \tag{3}$$

where φ_i and ϵ_i are the volume fraction and dielectric permittivity of the ith component, respectively (Guéguen and Palciauskas, 1994).

To determine the effective conductivity σ^* of a mixture of several components, we chose to calculate the average of two models. First, we assumed that the mixture could be described by resistances in series, and secondly, by resistances connected in a parallel circuit. It is well-known that these two models provide upper and lower bounds of effective conductivity (Guéguen and Palciauskas, 1994). The resulting expression of σ^* becomes

$$\sigma^* = \frac{1}{2}\left[\left(\sum_i \frac{\varphi_i}{\sigma_i}\right)^{-1} + \sum_i \varphi_i \sigma_i\right]. \tag{4}$$

Guéguen and Palciauskas (1994) mentioned that a self-consistent model does not model accurately the low-frequency conductivity of sedimentary rocks. A self-similar model — such as that proposed by Sen et al. (1981) — probably determines better the effective properties of sedimentary rocks. However, this model allows only the modeling of a two-phase medium. Therefore Equation 3 will be used for calculation of effective dielectric permittivity, but the results may not quantify the real values correctly.

Figure 6 shows the effective velocity of an effective medium that

Table 1. Electromagnetic properties of some relevant earth materials. (After Landau-Boernstein, 1982; Davis and Annan, 1989; and Guéguen and Palciauskas, 1994.)

Material	ϵ_r	σ (ms/m)	f_s = 50 MHz V (m/ns)	f_s = 50 MHz d_s (m)	f_s = 100 MHz V (m/ns)	f_s = 100 MHz d_s (m)	f_s = 200 MHz V (m/ns)	f_s = 200 MHz d_s (m)
Air	1	0	0.29	–	0.29	–	0.29	–
Fresh water	80	0.5	0.03	8.0	0.03	5.6	0.03	3.99
Shale	5–15	1–100	0.09	0.79	0.09	0.54	0.09	0.40
Dry sand	3–5	0.01	0.15	56.4	0.15	39.89	0.15	28.21
Limestone	4–8	0.5–2	0.12	8.0	0.12	5.64	0.12	3.99
Clays	5–40	2–1000	0.03	0.21	0.04	0.15	0.04	0.11
Calcite	7–8	2×10^{-9}						
Quartz	4.5–4.6	2×10^{-10}						

consists of porous limestone saturated to different degrees with water and air, after Equation 1a. Figure 6 shows that effective velocity depends strongly on water content, a well-known fact quantified by Topp et al. (1980) and Robinson and Friedman (2003), among others. From measurements deep in cracks at Turtle Mountain water is known to be present, but the fractures are not saturated (N. Iverson, personal communication). Accordingly, the effective velocity should differ from standard values. This fact also requires that migration velocities be chosen carefully, and tabulated values are not necessarily reliable.

In highly conductive materials, the shallow penetration reduces the feasibility of GPR imaging significantly. Where near-surface material is enriched with conductive clay minerals, the GPR method may not be applicable. The summit of Turtle Mountain is underlain mostly by limestone, so the values in Table 1 suggest that effects of dispersion are reduced substantially. However, the depth of penetration also is affected strongly by near-surface heterogeneities. Scattering at fractures and reflections at boundaries of strata of bedrock reduce the volume probed by ground-penetrating radar waves. For example, recent work by Lampe and Holliger (2003) shows that two variables can affect strongly the depth of penetration of GPR waves: (1) Topographic relief can cause insufficient antenna coupling to the ground, and (2) variations in permittivity and conductivity of near-surface material can have a strong effect on penetration. Therefore, values in Table 1 can be used only to estimate the upper limit of penetration depth.

Analysis of GPR data must be preceded by processing of the data, to correct for artifacts caused by wave propagation or errors introduced during acquisition of data. Generally speaking, processing of GPR data is similar to processing of seismic data; therefore, many algorithms and processing work-flows developed for seismic data can be applied directly. The processing scheme applied to data under discussion consisted of four steps: trace and static corrections, amplitude gain, frequency filtering, and migration.
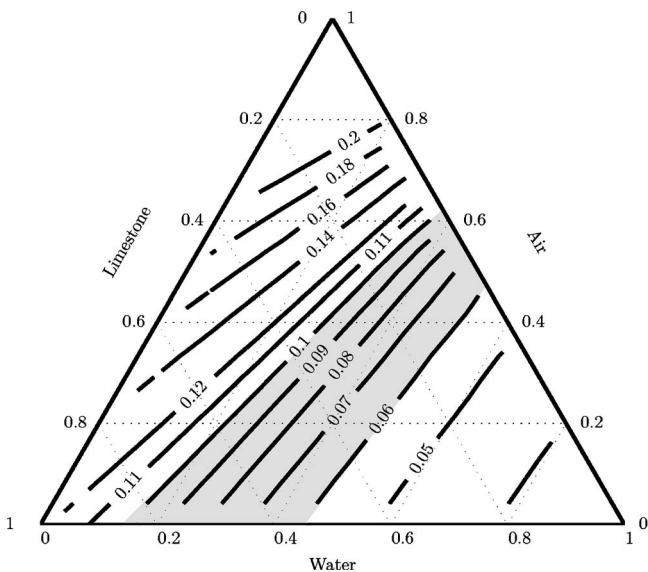

Figure 6. Effective electromagnetic velocities of a three-component mixture that consists of limestone, water, and air; components are expressed in volume fractions. Contours show lines of equal velocity (in m/ns). Area shaded gray shows the range of velocities that gave reasonable results for migration of GPR data sets.

The true propagation velocity of waves is a factor that is crucial for depth conversion, and particularly so for migration of data. The actual electromagnetic velocity can be determined experimentally in the field, if the area of study is underlain by subhorizontal strata of rock. Such experiments are called common-midpoint (CMP) surveys (Fisher et al., 1992); source and receiver antennae are moved away from each other, but the midpoint is at a fixed position. In CMP surveys, reflected waves appear at hyperbolae, from which velocities of subsurface materials can be approximated. Such an experimental determination was not possible on the fractured rock at Turtle Mountain's summit. Because we did not know the actual wave speed, we used a range of velocities to migrate the data; the most reasonable-looking data were used for further investigation. This testing of migration velocities mimics that method employed when migration trials are used to refine velocity structure in reflection seismology. For finding the best velocity for a migration algorithm, Fisher et al. (1992) described the following criterion: If the migration velocity is correct, the migrated image will be well focused. If the migration velocity is too low, diffraction hyperbolae will not collapse completely, but hyperbolic tails remain in the image. A velocity that is too large results in diffraction tails that extend from a diffractor toward shallower depths. The poor quality of data acquired at Turtle Mountain did not permit the direct use of this criterion. Instead, the criterion used is based on the observation that bedding planes visible at the surface and in the data (e.g., in Figure 7) are linear. Therefore, in migrated images, migration was considered to have been reasonable if features related to bedding planes (and possibly, fractures) appeared as linear entities.

The optimal window length for the automated gain control (AGC) routine was determined in a similar manner. First, a wide range for the window length was used. From the resulting data sets, we chose the one that resulted in events well separated along the trace. In amplifying zones where amplitudes are small, the recorded wavelet tends to be substantially distorted if the AGC window length is too short. On the other hand, if the window length is too large, individual events in the data are smoothed, and resolution is reduced.

Two of the three data sets described in following paragraphs were acquired on slopes along two flanks of Turtle Mountain; variation of the surface with respect to the slopes was of small scale. Where correction for these small variations in topography was required, the direct wave was flattened by shifting of traces in time. The first arrival in data is the air wave. Each trace in the data set was corrected to the time t = antenna separation/v_{air} (v_{air} = 0.29 m/ns). This implies that after migration, the vertical axis of the image is not true vertical depth with respect to the surface; it is a dimension that we refer to as normal depth — the direction normal to the surface of the slopes.

Experiment on the crest of Turtle Mountain, line PP′

A Malå-Ramac II GPR system with antenna frequencies of 50, 100, and 200 MHz was used in the surveys. Acquisition parameters of measurements are summarized in Table 2.

Before the extensive GPR survey program, we tested the feasibility of GPR of the summit of Turtle Mountain by a short survey. The main questions were: (1) Can GPR data be recorded on this material, and (2) will signals from high-frequency antennae penetrate deep enough to image fractures?

We used antenna systems of 100 and 200 MHz. Results of the 100-MHz survey are discussed in this paper. Data recorded with the 200-MHz antennae did not show significant structure. Probably, the highly fractured rock scattered wave energy so much that deep penetration was not achieved.

A simple initial processing stream was applied to the data. In most instances, the direct wave contained no significant information; therefore it was muted. Typically, DC-offsets are in GPR data; data were corrected for DC-offsets by applying a high-pass frequency filter. After correction for DC-offsets, amplitude gain was applied to recover energy lost to spherical spreading; a 38-ns long AGC window (50 samples) was used. A final band-pass filter (50 MHz–150 MHz) suppressed low-frequency amplitudes, which were introduced while gain was applied.

Line PP′ crosses Crack 1 and Crack 2 (Figure 4). Figure 5a is a photograph of Crack 1, which shows, that at the surface, the crack is approximately 1 m wide and nearly vertical. The exact dip is unknown. Figure 5a shows a pattern that is important in analysis of the three surveys conducted at Turtle Mountain: At this site, the crack is associated with a system of nearly vertical fractures that are normal to the bedding. However, in the central part of the photograph, the crack is shown to terminate at a fracture that is approximately parallel to bedding planes, but that extends past an offset of its original focus. These two fracture orientations — one parallel to bedding planes and the second perpendicular — form a system of fractures that is observed at numerous localities on Turtle Mountain (D. M. Cruden, personal communication). Orientations of these systems of fractures are indicated by red lines in Figure 5a.

Figure 5b shows the processed but unmigrated GPR data. The numerous reflections and diffractors in the image are evidence of the highly fractured bedrock. Because the reflectors are difficult to detect in the image, Figure 6c shows an interpretation of major reflectors in the data. The GPR image shows a noncontinuous pattern of Crack 1, similar to the pattern shown in Figure 6a. The reflector follows a certain direction in the t–x domain but terminates abruptly and continues thereafter, oblique to its initial direction.

GPR images were converted from the time domain to the normal depth domain by Kirchhoff migration (Yilmaz and Doherty, 1987). Because the true electromagnetic velocity of the fractured rock is not known, the data were migrated by using velocities in a wide range, from 0.06 m/ns to 0.16 m/ns, where 0.12 m/ns is the standard velocity of limestone (Table 1). From the set of migrated sections, those that looked the most reasonable were selected for further analysis. Migrations that involved velocities less than 0.10 m/ns delivered results that were considered to be adequate for the data. Typical overmigration artifacts appeared in the images when the velocity exceed-

ed 0.11 m/ns. Results of the effective-medium calculations in Figure 6 show that these velocities are indeed realistic for porous limestone that is saturated partly with water.

Figure 8 shows data migrated by using $v_{mig} = 0.08$ m/ns. The suspected signature of nearly vertical fractures (Figure 5b) is hardly visible in the migrated data. Imaging almost-vertical structures with wave-based methods such as GPR is difficult. Furthermore, numerous reflection and scattering at fractures and bedding planes result in images of numerous events in the GPR data. This complicates the interpretation significantly.
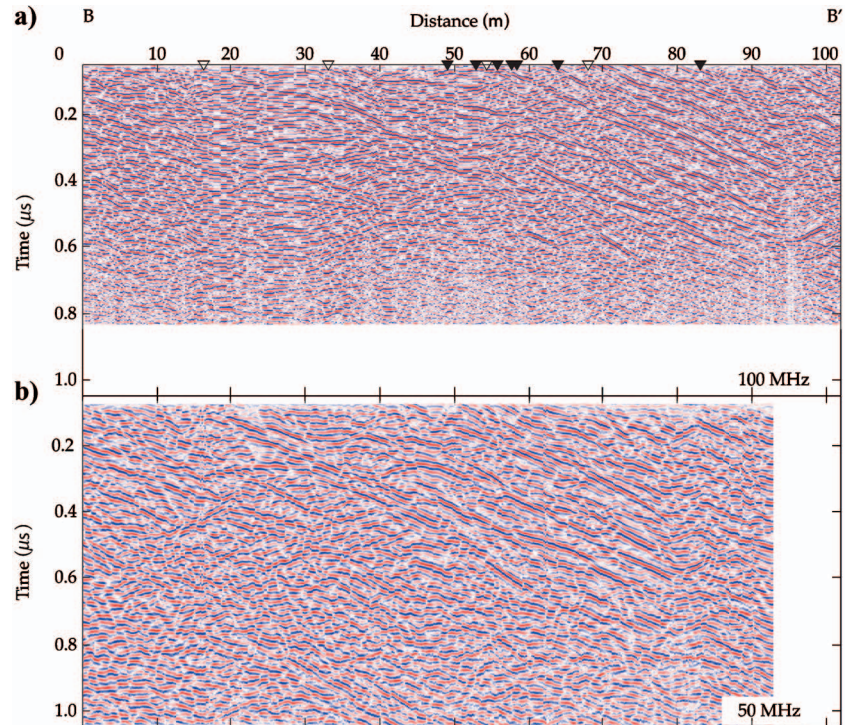

Figure 7. GPR data acquired at the west slope of Turtle Mountain (Figure 4); data were modified by basic processing. (a): Processed 100-MHz data. Filled and open triangles indicate locations of fractures at the surface, along the profile. Black triangles indicate fractures visible at the surface, on the line of profile; white triangles indicate fractures at the surface, but to the left or right of the line of profile. (b) Processed 50-MHz data. In both profiles, bedding planes are shown as coherent events that dip from left to right.

Table 2. Parameters for acquisition at GPR measurements at Turtle Mountain.

Survey	f_s (MHz)	Length (m)	Δx (m)	Δt (ns)	Comments
PP′	100	40	≈0.2	0.76	Line crosses two prominent cracks at approximately 10 and 22 m, respectively.
A′A	100	102	0.2	1.25	Main survey
B′B	50	93	0.2	0.93	—
C′C	100	30	≈0.2	0.93	Steep terrain made consistent measurements impossible.

Measurements on the West Slope of Turtle Mountain, lines A′A and B′B

The main survey to image bedding planes, steep fractures, and fissures was on Turtle Mountain's west slope. GPR surveys using 50- and 100-MHz antennae were conducted to acquire lines A′A and B′B (Figure 4). The surveyed area is the site of a rock avalanche the surficial material is mainly limestone scree. Differential GPS measurements indicated that this slope is approximately 29°. The relative angle between possibly near-vertical fractures and the surface is less than 90°, so imaging these fractures using GPR is less problematic then if the surface were level. However, the major fractures seen in the borehole most likely are not detectable in these surveys because their dip relative to the survey surface is approximately 90°. Lines A′A (100 MHz) and B′B (50 MHz) each were approximately 100 m long, and each crossed several fractures that were clearly visible at the surface.

Figure 9 shows the GPR data after muting of the direct wave, after amplitude gain, and after band-pass filtering. These parameters were used to process the 100-MHz antenna data: The AGC window length was 62.5 ns; the band-pass filter ranged from 50 MHz to 150 MHz. Parameters used to process the 50-MHz antenna data were 46.5 ns for the AGC window length and a band-pass frequency of 20 MHz to 100 MHz. Filled triangles at the top of Figure 9 indicate locations where fractures were visible at the surface. Open triangles indicate fractures that were visible on both sides of the profile location, but the intersections of such fractures with the line could not be determined because sand and pebbles concealed the fractures. The 100-MHz data (Figure 7a) show many details that probably resulted from reflection and scattering within the broken rocks or at bedding planes. Consequently, the main features in the data — such as coherent reflectors — are rather difficult to detect. They are clear in the 50-MHz data (Figure 7b). Depth of wave propagation is also greater for the low-frequency antennae, because for later arrivals, stronger amplitudes are recorded. For these reasons, and for brevity and clarity, the following analysis is based on 50-MHz data.

Subsequently, Kirchhoff migration was applied to the 50-MHz data and the 100-MHz data. As before, several constant-migration velocities were used, in the range from 0.06 m/ns to 0.12 m/ns. Some of these results are shown in Figure 9; they are for the 50-MHz data. Parameters for the migration algorithm were chosen so that in the migrated section a maximum normal depth of 40 m could be achieved. For a low velocity of 0.07 m/ns (Figure 9, second panel), the recoded time series is not long enough to reach the depth of 40 m after migration. Therefore, information only to a depth of approximately 36 m is available for this migration.

Crest slope experiment, line C′C

This survey was carried out on a steep portion of the slope west of the main crest (Figure 4, line C′C). Figure 10a shows that bedding is parallel to the slope on this part of the mountain. The steep slope required that the antenna operator be secured by ropes. At this site consistent measurements were difficult to obtain. Measurements were taken as soon as the antenna operator could hold the instrument steady for a short time. The positioning of antennae and the acquired data therefore are inaccurate to some degree. Nevertheless, the profile is included here because at this site bedrock is extremely fractured and therefore is a useful target for GPR measurements.

A profile approximately 20 m long was acquired by using the 100-MHz antenna system. The data, after basic processing, are shown in Figure 10b. Numerous events in the data indicate that bedrock the mountain is probably fractured extensively. Two orientations of reflections are dominant. One is subparallel to the surface; it may be composed of reflections at bedding planes. The second, inclined from left to right, may be related to fractures.

The data were migrated by the Kirchhoff algorithm, with six migration velocities in the range of $v_{mig} = 0.06$ m/ns and $v_{mig} = 0.12$ m/ns. However, given the original data, the resulting images are of poor quality compared to the line that comprises A and B (Figure 9).

Given the complicated fractured structure of bedrock at this site, to decide to discriminate between images of fractures and artifacts of processing is difficult. An additional complication was the difficulty of collecting data.

INTERPRETATION

The migrated data in Figure 9 shows evidence of several linear coherent events. This contrasts with Figure 7 the results from line PP′ where detection of continuous events is very difficult. As a final step in the analysis, determination of the maximum depth and dip of these events was attempted. However, a unique answer could not be found, because the true ambient propagation velocity of the electromagnetic waves is not known precisely. The two important parameters in construction of geomechanical models — depth and dip of fractures — depend on migration velocity (for example, see Figure 9, in which the three panels were migrated with different velocities). In these images, dip and the depth of features in the data depend strongly on migration velocity; this is apparent. This nonuniqueness adds significant uncertainty to results of the interpretation. To address this uncertainty, we determined separately the shapes of coherent linear events in each data set migrated with different velocities. Then all the inferred dips were combined and analyzed statistically.

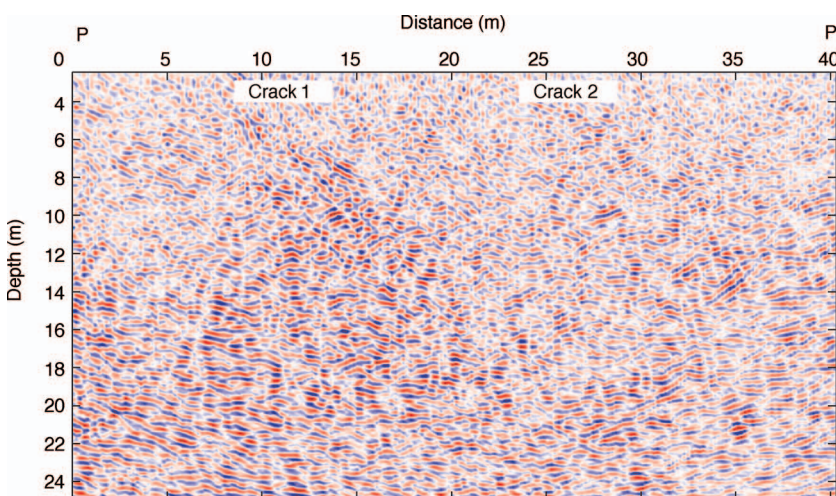The following interpretation concerns analysis

Figure 8. GPR data acquired along line PP′, after Kirchhoff migration (v = 0.08 m/ns).

of migrated data of the 50-MHz profile acquired at the west slope, the 100-MHz survey along line C′C, and 100-MHz data from line PP′. To follow a reflector in the migrated data is generally difficult, because the rock mass seems to be highly fractured. Many reflectors are discontinuous and are intersected at numerous places by other reflections. The true position of a point on a reflection commonly must be assumed. Therefore, in the events inferred from the migrated data, significant uncertainty must be taken into account.

Migrated data acquired at the west slope show two basic reflection patterns, with different dips (Figure 11). A dominant system of reflectors shows apparent dip of approximately 54° to 59° southwestward (Figure 11b). Also, this is approximately the dip of bedrock at this part of Turtle Mountain (Spratt and Lamb, 2005). Therefore, these reflectors probably are not evidence of fractures. A counterargument is that these discontinuous reflections — which at many places are intersected by reflectors that are almost horizontal — indi-

cate that strata are fractured along bedding planes. Although the reflections could have been produced at bedding planes, the strength of these events and their good correlation with Cracks 1 and 2 indicate that they could be the signatures of fractures. Indeed, one might expect even fractures and bedding planes to be strongly correlated, the latter having potential as inherent zones of weakness.

Figure 11a shows a map of all fractures combined, which were interpreted from the sets of migrated data. The dominant pattern, with average dip of approximately 58°, is apparent. Also, between 20 and 40 m along the profile — at approximately 10 to 30 m deep — numerous events are nearly horizontal.

Figure 11b shows the relative numbers of apparent dips of all reflectors depicted in Figure 11a. The length of each segment represents the proportion of dipping reflectors per 10° interval. This diagram also shows that the southwestward dip of bedding dominates the reflections in the GPR survey of the west slope, but a significant
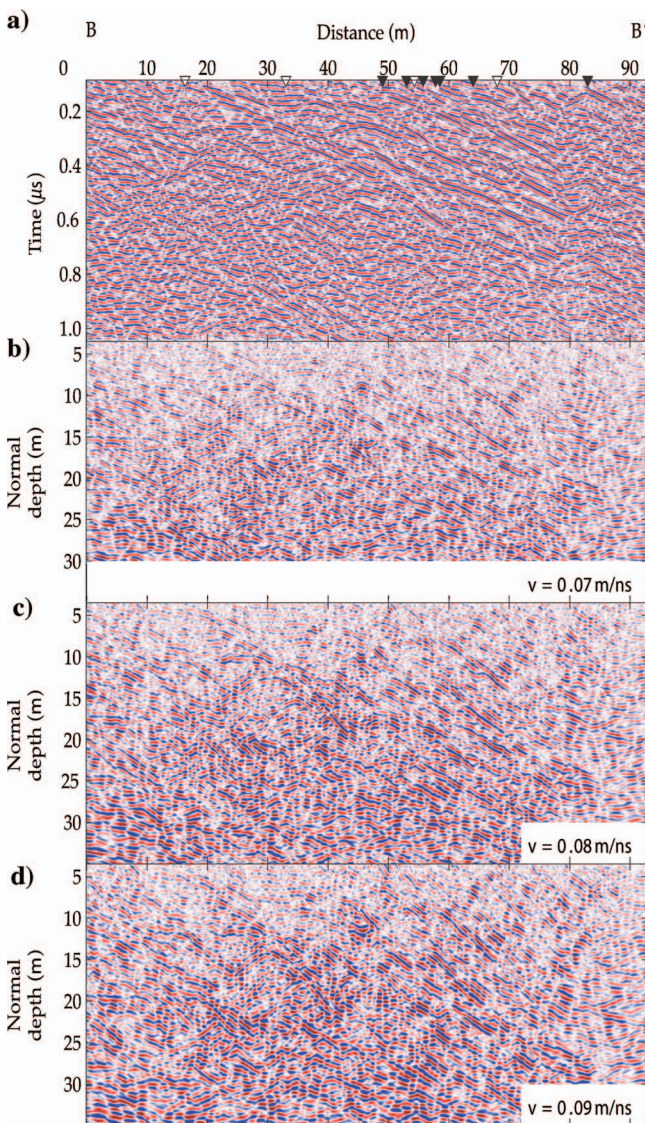

Figure 9. Three migrations of 50-MHz data collected on the west slope (Figure 4). (a) Unmigrated data; (b) $v_{mig} = 0.07$ m/ns; (c) $v_{mig} = 0.08$ m/ns; (d) $v_{mig} = 0.09$ m/ns. The open and filled triangles indicate suspected and known positions of fractures at the surface, respectively.
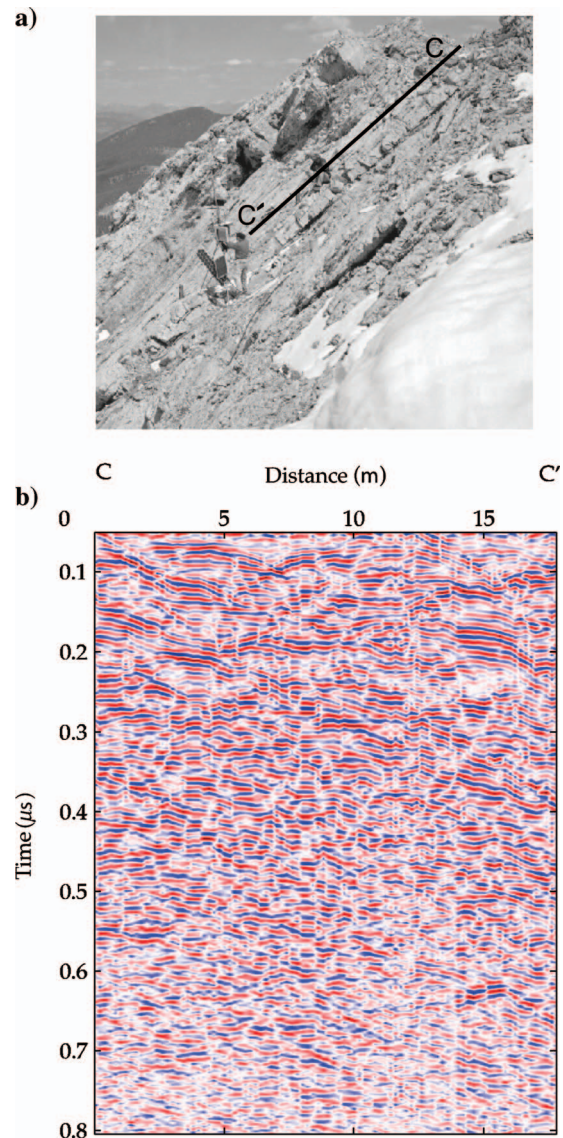

Figure 10. Measurement with 100-MHz antennae. (a) The approximate location of the survey (see profile C′C, Figure 4). (b) GPR data after basic processing. Strata are shown clearly, subparallel to the surface.

number of reflections show evidence of nearly horizontal dip.

Figure 11 shows that at positions near 10 m and between 20 m and 50 m profile length, no evidence of bedding planes or fractures could be inferred from the migrated data at shallow depth (zones marked by ⊗). These positions coincide with locations of scree beds on the west slope. In such accumulations of loose rock, distinguishable interfaces between strata of competent rock do not exist. Instead, numerous events with no distinctive signatures dominate the GPR image. The migrated GPR data suggest that locally the scree is as thick as 10 m, as measured normal to the surface of the slope.

Figure 12a shows results from a similar interpretation of the GPR survey data along line CC′. The slope of the land surface is approximately 35°. Figure 10a shows that at this locality, strata dip subparallel to the surface. This fact explains the numerous reflectors that are subparallel to the slope (Figure 12a). In addition, steep-dipping

events are visible in the migrated data (Figure 12a): these indicate strongly fractured rock. As described above, to acquire equally spaced GPR data at this site was not possible. Therefore, the data contain errors in the shapes of fractures, and hence in the depths and apparent dips of fractures. As with the data acquired at the west slope (line B′B), reflections that portray bedding appear to be dominant in the GPR images along line CC′. This is demonstrated by the dominant reflector dip of 35° (Figure 12b).
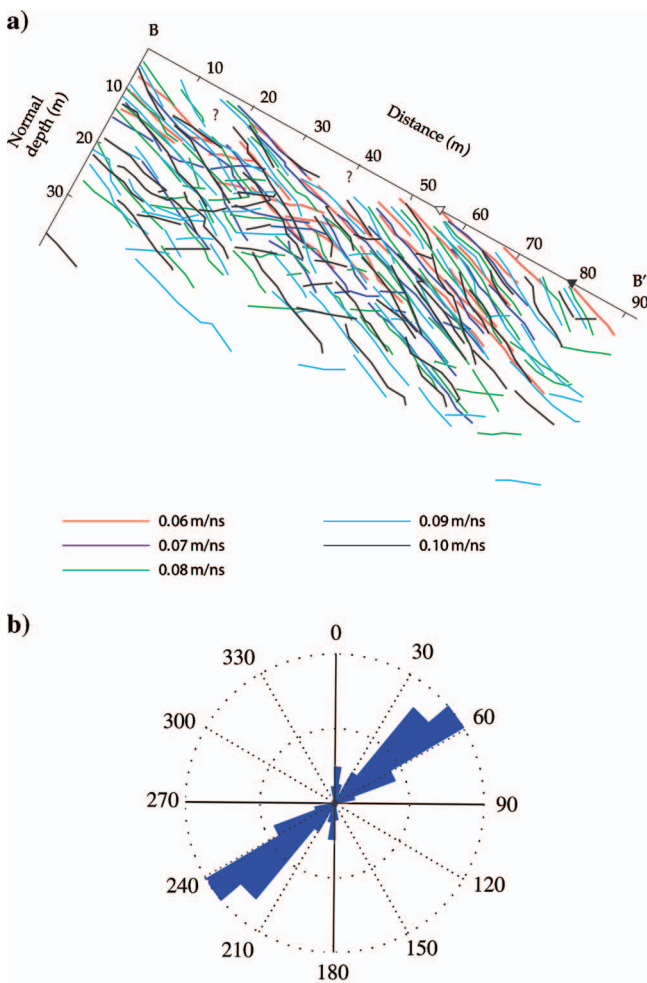

Figure 11. (a) Near-surface fractures inferred from migrated 50-MHz GPR data. Axes were rotated so that the "distance" axis represents the inclination of Turtle Mountain's west slope (29°). Locations of Crack 1 and Crack 2 are marked by solid and open triangles, respectively. (b) Apparent dips (in degrees) of fractures in the shallow subsurface. The line labeled 180-to-0 represents the horizontal plane along profile BB′. The perspective is southeastward (Figure 4); fractures show apparent dip southwestward. Scale for relative frequencies of fractures is based on normalization by the maximal frequency. Dotted lines that show relative frequency are one-half the normalized maximum, and the normalized maximum.
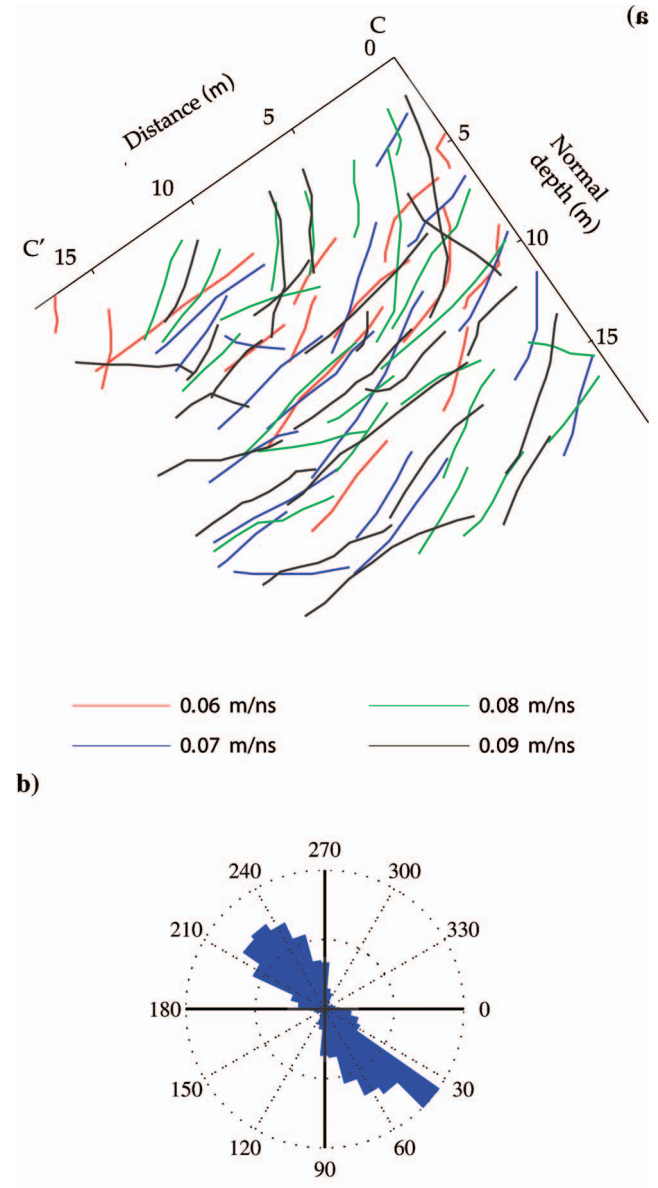
Figure 12. (a) Fractures and bedding planes detected in the sets of migrated data, line CC′. Axes were rotated so that the "distance" axis shows the slope of the surface along line CC′ (35°). (b) Apparent dips (in degrees) of fractures in the shallow subsurface. The line labeled 180-to-0 represents the horizontal plane along the CC′. The perspective is slightly westward (Figure 4); fractures and bedding planes show apparent dip westward. Scale for relative frequencies of fractures is based on normalization by the maximal frequency. Dotted lines that show relative frequency are one-half the normalized maximum, and the normalized maximum.

Figure 13 shows the interpretation of line PP′. The four images analyzed resulted from migrations with velocities in the range of 0.07 m/ns to 0.10 m/ns. However, this interpretation must be made carefully, because the GPR images are of very poor quality; therefore, substantial uncertainty is embedded in this analysis. In Figure 13, between 0 and 20 m, several reflectors dip at approximately 28°, generally northward to northeastward. These reflectors are intersected by reflections with steeper dip, which impinge on the surface at around 10 m, profile distance. These events correlate well with the location of Crack 1 on the profile of line PP′ (compare Figures 13 and 4). The dip of this crack is in the range of 48° to 70° (Figure 13). A similar pattern of steep reflectors that is barely distinguishable is interpreted as being the signature of Crack 2. This set of reflections impinges on the surface in line PP′, at about 22 m.

Figure 13. Fractures and bedding planes, as inferred from four migrated GPR images for most of line PP′. Positions of Crack 1 and Crack 2 are indicated by solid and open triangles, respectively.

DISCUSSION AND CONCLUSIONS

Despite the rough terrain, the results of the GPR data acquired at Turtle Mountain hold promise for mapping fractures and bedding planes at the mountain's summit. Significant depth of penetration normal to the surface was achieved, especially with the low-frequency antennae. At some localities, the fracture system and bedding planes could be mapped to a depth of approximately 40 m (Figure 11). Many features readily were apparent in the raw data, and more features became clearly visible after basic processing of data. However, because the bedrock is highly fractured, the images contain many details in addition to the reflectors that are of principal interest.

Analysis of data collected from the crest of Turtle Mountain (Figures 5, 8, and 13) emphasizes the difficulty of imaging nearly vertical structures with ground penetrating radar. Events that appear in processed raw data (Figure 5b) are difficult to observe after data are migrated. The two main fractures dip almost vertically; therefore, they are difficult to record with zero-offset GPR acquisition systems. A possible explanation for this difficulty is that events in the unmigrated GPR data — which we related to Cracks 1 and 2 (Figure 5b) — are diffraction tails, the result of scattering at the tops of the cracks and not of reflections from deeper parts of the cracks.

In migrated data acquired at the west slope, a pattern of two consistent events was detected. This pattern was interpreted as a network of two fracture systems (Figures 9 and 11). A long line BB′, a system of fractures with average apparent dip of 54° ± 8° is dominant, in number of fractures and lengths of fractures. The long, linear coherence and the dips of these reflectors suggest that the reflectors are bedding planes. Uncertainty in measurement of dips originates from statistical analysis of the data and from the fact that data were migrated with a rather wide range of velocities. Use of several migration velocities results in a range of dips and depths of reflectors, which were combined before statistical analysis. Therefore, there is also a physical contribution to uncertainty of the average dip.

The second fracture system in rock at the west slope is composed of a smaller number of fractures. In this system, the average apparent dip is 2° ± 7°, nearly horizontal (Figure 11b). At the surface there is no evidence of these reflectors. The fact that these reflectors intersect the refl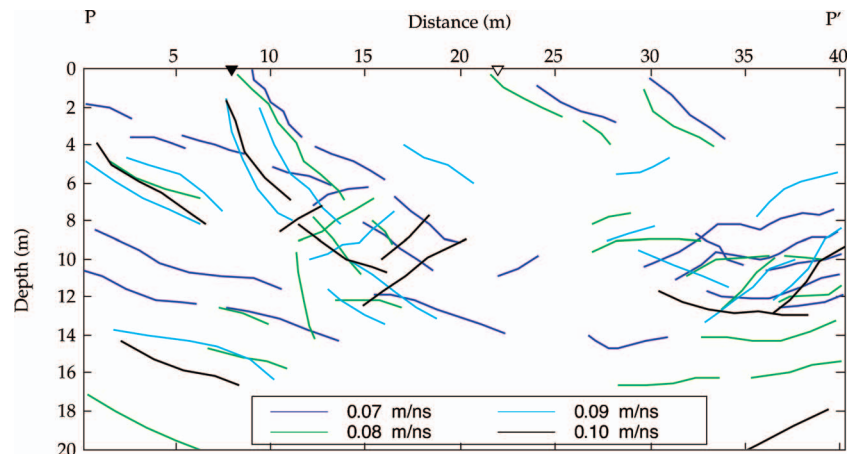ectors associated with bedding planes can be interpreted as evidence that these nearly horizontal reflectors are fractures within the bedrock.

In migrated sections, events commonly terminate at a fracture. In some instances, a reflector shows evidence of offset. The aerial photograph (Figure 4) and the image of Crack 1 (Figure 5a) show that the strikes of fractures vary abruptly. However, at the summit of Turtle Mountain rocks are fractured along bedding planes (Cruden and Krahn, 1973; Benko and Stead, 1998). We could not determine whether the offset reflections are associated with bedding planes or with fractures.

An extensive pattern of fractures is present also at the mountain's crest, as the GPR data acquired at line CC′ reveal (Figures 4 and 12). Most reflectors are parallel to the surface; therefore, they are interpreted as being images of strata of bedrock. Parallel reflections are detectible to the depth of approximately 20 m, normal to the surface. However, embedded in the data is evidence of fractures that are almost vertical.

Analysis of the data showed that subsurface structure can be mapped in such a rough environment. Structures in the migrated data of lines BB′ and CC′ that probably are related to bedding planes correlate well with observations of bedding at the surface. If the reflectors truly are segmented, and if these segments are evidence of highly fractured rock, then the data show that fractures extend to depths of as much as 30 m, as measured normal to the surface. Along line BB′, the pattern of the data suggests a secondary reflector that has no signature at the surface (Figure 11). These reflections may be evidence of fractures.

Images in two patterns — one of 54° ± 8° and one at 2°, approximately horizontal (Figure 11b) — reflect the two sets of joints described by Cruden and Krahn (1973). The GPR image obtained for line CC′ clearly shows strong reflections parallel to slope of the surface (Figure 12), which is subparallel to dip of bedrock. These events result from reflection at bedding planes. However, extensional cracks follow the dip of the bedding planes. We were able to observe such reflections to depths of approximately 15 m. Additionally, some reflectors dip almost vertically (Figure 12a). Given the poor quality of data, to infer very reliable information about these reflectors is difficult. However, because the dip is almost vertical, such fractures may pose a significant risk for rock slides at this part of the mountain.

Migrated GPR data are the most important for further application. For example, shapes of fractures, determined from such GPR images, might be used in geomechanical modeling for study of slope stability. However, migration must be performed carefully and with proper choice of input parameters — primarily migration velocity. To perform velocity measurements at Turtle Mountain was not possible through acquisition of CMP measurements, for example, because the rock mass is extensively fractured. Instead, several attempts at migration were made, by use of a wide range of velocities. The effective-medium calculations of in situ velocity showed that the selected velocities would be reasonable for porous limestone partially saturated with water. From the sets of migrated data, those chosen for further analysis were the sets that appeared to be visually reasonable.

Is the observation of considerably reduced migration velocity informative about near-surface in situ conditions of Turtle Mountain? Calculations for an effective medium shown in Figure 5 suggest that the low velocities observed may result from water in the porous, fractured limestone. That water can reduce the stability of slopes is a well-known fact. Therefore, future work could be directed to the extraction of information from GPR data such as that acquired at Turtle Mountain. The work by Wang and Oristaglio (2000) about constructing permittivity and conductivity maps from GPR data could provide guidance for such analyses.

ACKNOWLEDGMENTS

REFERENCES

Allan, J. A., 1931, Report on stability of Turtle Mountain, Crowsnest District, Alberta: Technical report, Dept. of Public Works, Edmonton, Alberta. Alberta Provincial Archives.

——, 1933, Report on stability of Turtle Mountain, Alberta, and survey of fissures between North Peak and South Peak: Technical report, Dept. of Public Works, Edmonton, Alberta. Alberta Provincial Archives.

Benko, B., and D. Stead, 1998, The Frank Slide: A reexamination of the failure mechanism: Canadian Geotechnical Journal, **35**, 299–311.

Cruden, D., and J. Krahn, 1973, A re-examination of the geology of the Frank Slide: Canadian Geotechnical Journal, **10**, 581–591.

Davis, J., and A. Annan, 1989, Ground-penetrating radar for high-resolution mapping of soil and rock stratigraphy: Geophysical Prospecting, **37**, 531–551.

Fisher, E., G. McMechan, A. Annan, and S. Cosway, 1992, Examples of reverse-time migration of single-channel ground-penetrating radar profiles: Geophysics, **57**, 577–586.

Goodman, D., Y. Nishimura, and J. Rogers, 1995, GPR time-slices in archaeological prospection: Archaeological Prospection, **2**, 85–89.

Grasmueck, M. P., 1996, 3-D ground-penetrating radar applied to fracture imaging in gneiss: Geophysics, **61**, 1050–1064.

Grodner, M., 2001, Delination of rockburst fractures with ground penetrating radar in the Witwatersrand Basin, South Africa: International Journal of Rock Mechanics, **38**, 885–891.

Guéguen, Y., and V. Palciauskas, 1994, Introduction to the physics of rocks: Princeton University Press, 392.

Hammon, W., G. McMechan, and X. Zeng, 2000, Forensic GPR: Finite-difference simulations of responses from buried human remains: Journal of Applied Geophysics, **45**, 171–186.

Hoek, E., and J. Bray, 1981, Rock slope engineering: Institution of Mining and Metallurgy, London, 3rd edition, 360.

Knödel, K., H. Krummel, and G. Lange, 1997, Geophysik: Springer Verlag.

Lampe, B., and K. Holliger, 2003, Effects of fractal fluctuations in topographic relief, permittivity and conductivity on ground-penetrating radar antenna radiation: Geophysics, **68**, 1934–1944.

Landau-Boernstein, H., 1982, Zahlenwerte und Funktionen aus Naturwissenschaft und Technik, Gruppe V: Physikalische Eigenschaften der Gesteine: Springer Verlag.

Marshak, S., and G. Mitra, 1988, Basic methods in structural geology: Prentice Hall.

Moldoveanu-Constantinescu, M., and R. Stewart, 2004, 3D ground penetrating radar surveys on a frozen river lagoon: Recorder, **29**, 32–35.

Rashed, M., D. Kawamura, H. Nemoto, T. Miyata, and K. Nakagawa, 2003, Ground penetrating radar investigations across the Uemachi fault, Osaka, Japan: Journal of Applied Geophysics, **53**, 63–75.

Read, K., W. Savigny, F. Oboni, D. Cruden, and C. Langenberg, 2000, Geotechnical hazard assessment of the south flank of Frank Slide, Hillcrest, Alberta: Geotechnical hazard assessment of the south flank of Frank Slide, Hillcrest, Alberta: CSEG annual convention, 4.

Robinson, D., and S. Friedman, 2003, A method for measuring the solid particle permittivity or electrical conductivity of rocks, sediments, and granular materials: Journal of Geophysical Research, **108**, B2, ECV 5–1 to 5–9.meas

Sen, P. N., C. Scala, and M. H. Cohen, 1981, A self-similar model for sedimentary rocks with application to the dielectric constant of fused glass beads: Geophysics, **46**, 781–795.

Spratt, D. A., and M. A. Lamb, 2005, Borehole data interpretation and orientations (Report WP15b), University of Calgary.

Stevens, K. M., G. S. Lodha, A. L. Holloway, and N. M. Soonawala, 1995, The application of ground penetrating radar for mapping fractures in plutonic rocks within the Whiteshell Research Area, Pinawa, Manitoba, Canada: Journal of Applied Geophysics, **33**, 125–141.

Stewart, R., H. Bland, J. Thurston, and K. Hall, 2004, The surface microseismic monitoring system on Turtle Mountain, Alberta: Recorder, **29**, 42–44.

Topp, G. C., J. Davis, and A. Annan, 1980, Electromagnetic determination of soil water content: Measurements in coaxial transmission lines: Water Resources Research, **16**, 574–582.

Wang, T., and M. Oristaglio, 2000, GPR imaging using the generalized Radon transform: Geophysics, **65**, 1553–1559.

Willenberg, H., T. Spillmann, K. F. Evans, H. R. Maurer, E. Eberhardt, and S. Loew, 2004, Geological, geophysical and geotechnical investigations into the internal structure and kinematics of an unstable, complex sliding mass in crystalline rock: International Symposium on Landslides, 489–494.

Yilmaz, O., and S. M. Doherty, 1987, Seismic data processing series: Investigations in Geophysics, 2, SEG.

Zeng, X., and G. McMechan, 1997, GPR characterization of buried tanks and pipes: Geophysics, **62**, 797–806.